AGH

ISSN 2543-9901

JOURNAL OF CASTING & MATERIALS ENGINEERING

AGH UNIVERSITY OF SCIENCE AND TECHNOLOGY
FACULTY OF FOUNDRY ENGINEERING

QUARTERLY
Vol.4 No. 2/2020

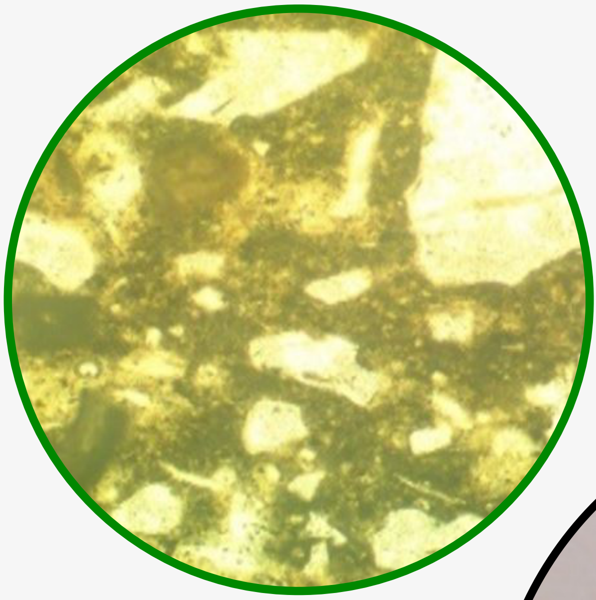

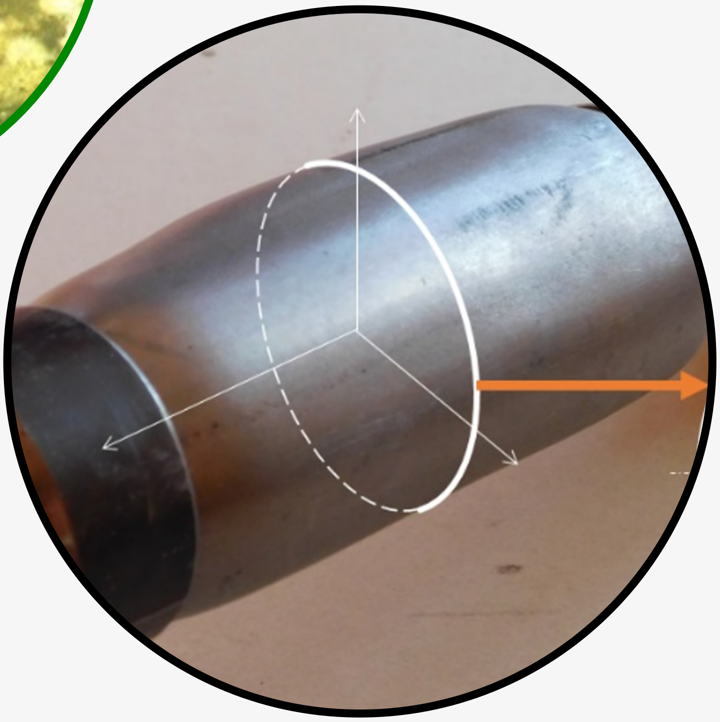

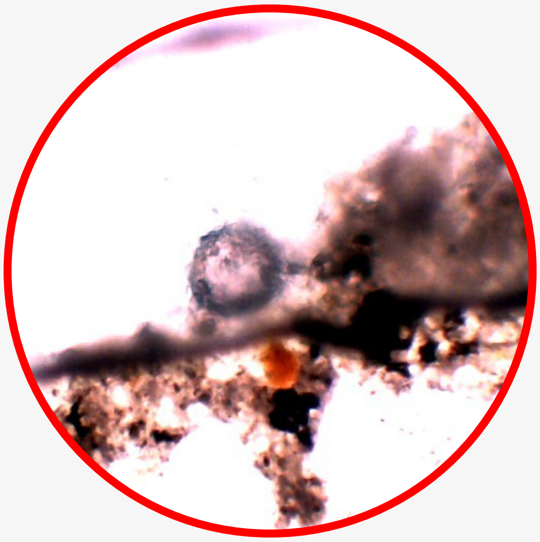

100 YEARS OF AGH UST

JCME

AGH UNIVERSITY OF SCIENCE AND TECHNOLOGY PRESS KRAKOW 2020

Editor-in-Chief of AGH University of Science and Technology Press
Jan Sas

The articles published in the Journal of Casting & Materials Engineering have been given a favorable opinion by the rewievers designated by the Editorial Board.

www:
https://journals.agh.edu.pl/jcme/

AGH UNIVERSITY OF SCIENCE AND TECHNOLOGY PRESS KRAKOW 2020

Wydawnictwa AGH (AGH University of Science and Technology Press)
al. A. Mickiewicza 30, 30-059 Kraków
tel. 12 617 32 28, 12 638 40 38
e-mail: redakcja@wydawnictwoagh.pl
http://www.wydawnictwa.agh.edu.pl

Contents

Journal of Casting & Materials Engineering Vol. 4 No. 2 (2020) 23–28
https://doi.org/10.7494/jcme.2020.4.2.23

An Evaluation of Combustion Kinetics for the Synthesis Reaction of the Reinforcing Phase During Casting

Tomasz Wiktor, Sebastian Sobula*, Andriy Burbelko, Michał Ptasznik

AGH University of Science and Technology, Faculty of Foundry Engineering, Reymonta St. 23, 30-059 Krakow, Poland
**e-mail: sobula@agh.edu.pl*

Received: 30 December 2019/Accepted: 19 June 2020/ Published online: 30 June 2020
This article is published with open access at AGH University of Science and Technology Press

Abstract

The computer modeling of the solidification process in castings with local composite reinforcement (LCR) obtained as a result of *in situ* reactions of self-propagating high temperature synthesis (SHS) is difficult due to limited data on the thermo-physical parameters of exothermic effects and the kinetics of the synthesis reaction. In the present study, Hadfield cast steel casting was manufactured with LCR containing titanium carbide particles obtained *in situ* by the SHS method. Reaction kinetics of titanium carbide synthesis in the composite casting were determined on the basis of temperature measurements in the area of LCR during the process. For the estimation of the reaction, the Fourier Thermal Analysis method was used. The paper presents the results of temperature measurement and the results of the calculation of SHS reaction kinetics. It was found that the reaction time under the conditions of the analyzed casting is below 3 s.

Keywords:

MMC, SHS reaction kinetics, Fourier thermal analysis, computer modelling

1. INTRODUCTION

The creation of local composite reinforcements (LCR) zones with increased hardness and resistance to abrasion allows the extension of the working time of iron alloy castings. One of the most well-known methods of achieving this effect is the synthesis of the reinforcing phases as a product of an exothermic, chemical reaction occurring *in situ* in the selected areas of the casting. Reinforcing particles are formed during the reaction of the Self-Propagating High-Temperature Synthesis process (SHS) in a component composed of compressed powders containing synthesis reaction reagents attached to the mold cavity.

The manufacturing and replacement of the ordinary cast parts with cast components with local composite zones is one of the important ways of the evolution of modern casting. Composite castings are characterized by the high hardness of the local composite reinforcements (LCR), which directly influences the lifetime of these castings. One popular method to obtain LCR is by using *in situ* SHS processes during casting. This method makes it possible to obtain very hard localized composite zones reinforced with carbide particles. Correct selection of raw material composition for SHS reaction provides a hardness of reinforced sections at the level from HV650 to HV900 [1, 2].

The composition of the raw materials for the manufacturing of local composite zones includes both active components (powders of the carbide-forming elements, such as titanium, tungsten, molybdenum and carbon powder) and a moderator. The moderator is used to improve dimensional stability and control of SHS reaction. The chemical composition of the moderator is usually similar to the base alloy chemical composition [3].

The energy which is released during the exothermic synthesis of reinforced particles in areas of LCR influences the temperature field in casting and in the mold. The thermal effect of synthesis depends on the weight fraction of reagents and the moderator in compact. The control of the moderator weight fraction is a fundamental problem during LCR synthesis in castings.

If the amount of active ingredients is small and the amount of moderator is large, the SHS reaction can be terminated before completion, due to the small amount of heat generated by the synthesis. This results in low infiltration, poor bonding between the base alloy and LCR, and finally low properties in the local area of the composite. Otherwise, when the weight fraction of the reagent is relatively large, the amount of heat released as a result of the reaction to the surrounding volume causes the formation of coarse reinforcement particles, which are dispersed in the volume of the casting.

The use of an excessive amount of active ingredients means that the synthesis temperature may clearly exceed the initial temperature of the liquid steel. Such an example is shown in Figure 1: the changes of temperature are presented in the SHS reaction zone (LCR1) and in the base carbon cast steel casting (L25GS, i.e. according to PN standard) at the distance of 10 mm from surface of compact. In the cited experiment, green compact was made from titanium and carbon powders in stoichiometric ratio. A high rate of temperature increase is visible after the beginning of the synthesis reaction in the component containing substrates for the formation of titanium carbide. Additionally, this heat affects solidification and leads to the formation of hot spots in the local area of the composite.

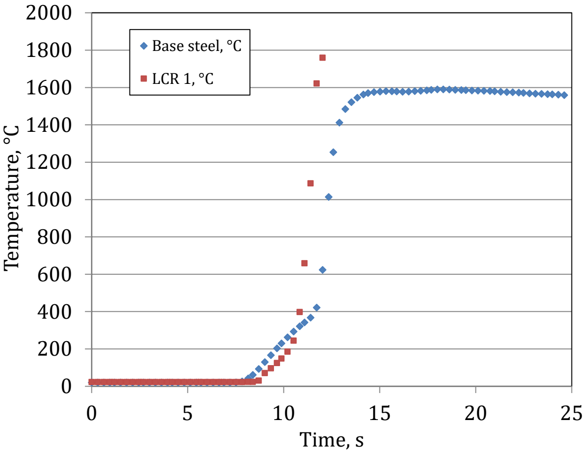

Fig. 1. Temperature changes in steel casting and in the SHS reaction zone [4]

A significant amount of thermal energy introduced in these places into the casting must be taken into account when developing the technology for producing such castings. Designing the technological process of the production of LCR castings encounters difficulties related to limited access to thermo-physical data and data concerning the kinetics of the fusion reaction of reinforcing phases. Problems related to the measurement and evaluation of exothermic material parameters in laboratory and industrial conditions are presented in [5–7].

The use of computer-aided analysis of cooling curves is known in foundry practice for measuring of exothermic transformation kinetics. The Fourier-Thermal Analysis (FTA) method makes it possible to estimate the intensity of exothermic processes occurring in the local volume of the analyzed material. The intensity of the thermal effect using FTA is assessed by comparing the rate of temperature change with a base line calculated from the Laplace operator of temperature.

The fundamentals of the Fourier Thermal Analysis (FTA) method has been presented in [8, 9]. In these papers, FTA has been used to determine the kinetics of gray cast iron solidification in the local region. Later, the FTA method has been successfully used to characterize the solidification process for various metal alloys, such as: aluminum-based materials [10–15], magnesium alloy [16], different Pb-Sb alloys [17], and for cast-composites [18]. As it has been proven in [19], the FTA method can also be used to analyze the kinetics of thermal decomposition of resin binders intended for use in molding sands.

In this paper, the FTA method was used to assess the thermal effect of an exothermic SHS reaction in the LCR area in steel castings.

2. THEORETICAL BASIS

A non-steady state temperature field in the medium with an exothermic or endothermic reaction can be described by the Fourier equation which includes a heat source:

$$\frac{\partial T}{\partial t} = a\nabla^2 T + \frac{\dot{Q}}{c} \tag{1}$$

where:

$\partial T/\partial t$ – the rate of material cooling, K/s,
a – the thermal diffusivity, m^2/s,
$\dot{Q}$ – volumetric heat generated or absorbed by the substance matter during the reaction, W/m^3,
c – the volumetric specific heat, $J/(m^3K)$,
∇^2 – the Laplace operator ($\nabla^2 = \partial^2/\partial x + \partial^2/\partial y + \partial^2/\partial z$),
T – temperature, K.

For the estimation of heat generation rate, at the first stage of FTA the *apparent value* of the temperature diffusivity of the substance (a_{av}, m^2/s) should be determined on the basis of the temperature measurement at several points of the analyzed sample. This value is determined by dividing the rate of temperature changes by Laplacian of the temperature $\nabla^2 T$:

$$a_{av} = \frac{\frac{\partial T}{\partial t}}{\nabla^2 T} \tag{2}$$

Outside the reaction zone, the apparent value of temperature diffusivity (a_{av}, m^2/s) is slightly dependent on the temperature. In the reaction zone, the changes are intense and irregular.

At the second stage of FTA, the interpolated value of the temperature diffusivity a_{int} should be estimated for the reaction period on the basis of the temperature diffusivity levels of the analyzed substance before (a_1) and after (a_2) the exothermic reaction. For precise analysis a_1 and a_2 values can be measured in laboratory conditions. In the case of approximate calculation, these parameters can be determined graphically from "a_{av}-time" diagram at the beginning and end of the range of irregular changes of the apparent temperature diffusivity.

Heat generation rate can be estimated based on the results of measurements using the equation:

$$\dot{q} = \frac{\dot{Q}}{c} = \left(a_{av} - a_{int}\right) \cdot \nabla^2 T \tag{3}$$

For the measurements, the temperature-time derivative and second spatial temperature derivative are replaced in the Equations (2) and (3) by proper central differential quotients.

Volumetric heat released as a result of the exothermic reaction should be calculated by temporal integration between the time instants of the reaction start (t_1) to reaction finish (t_2):

$$\Delta H = \int_{t_1}^{t_2} \dot{q}(\tau) \cdot c \cdot d\tau \tag{4}$$

Let as assume that changes of the volumetric specific heat of the analyzed substance with respect to the average value $\bar{c}$ are small during the reaction period. Under such conditions:

$$\frac{\Delta H}{\bar{c}} \approx \int_{t_1}^{t_2} \dot{q}(\tau) \cdot d\tau \tag{5}$$

and $\dot{q}$value (measured by K/s) may be used for the indication of the reaction rate. In this case, the conversion level of the analyzed exothermic reaction *f* may be calculated by the numerical integration of this value by time in the following way:

$$f(t) = \frac{\int_{t_1}^{t} \dot{q}(\tau) d\tau}{\frac{\Delta H}{\bar{c}}} \tag{6}$$

where t_1 and t_2 mean the time instants of the reaction beginning and end.

Extent of the SHS reaction can be calculated on the basis of Equations (5) and (6) as:

$$f(t) = \frac{\int_{t_1}^{t} \dot{q}(\tau) d\tau}{\int_{t_1}^{t_2} \dot{q}(\tau) d\tau} \tag{7}$$

3. EXPERIMENTAL PART

In the experimental part, measurements of the temperature field were carried out. The scheme of experimental casting is presented in Figure 2. The base casting was made of Hadfield cast steel (grade GX-120Mn13 according to PN-EN 10349:2009 standard). The compact, which was made of pressed powders, was attached to the mold cavity surface. The compact was made from titanium and carbon powders (44 μm) in amount of 50 wt.% and a moderator which balanced the weight.

The chemical composition of the moderator corresponded to the composition of Hadfield cast steel, which was selected as the base material. The strict chemical composition of the compact is shown in Table 1.

Table 1
Chemical composition of compact, wt.%

C	Ti	Fe	Mn	Si
9.1	41.5	38.7	10.5	0.3

The diameter of the compact was 30 mm, and the height was 10 mm. Compaction was carried out at a pressure of 450 MPa. In the compact, 3 thermocouples type S were installed with the step equal to 5 mm. Positions of the thermocouples are presented in Figure 2. All of the thermocouples were placed in quartz tubes with an external diameter of 3 mm. 10 mm wide plates of insulating material, made from aluminum silicates fibers, were mounted on the top and bottom sides of compact to minimize the vertical component of the heat flow in the LCR region.

Temperature measurement was performed with a multichannel Agilent 34970A data logger. The device performed temperature measurements at uniform time intervals of 288 ms. The obtained time step for recording measurements for each of the four thermocouples was 1.153 ms respectively.

The evaluation of the radial temperature gradient in the cylindrical compact was calculated using the central difference scheme for points located 2.5 mm (on the base of temperature measurement in the points R0 and R5) and 7.5 mm (on the base of temperature measurement in the points R5 and R10) from the compact axis of symmetry. In the center point of the compact, the constant temperature gradient equal to 0 K/m was assumed due to the axial symmetry of this element.

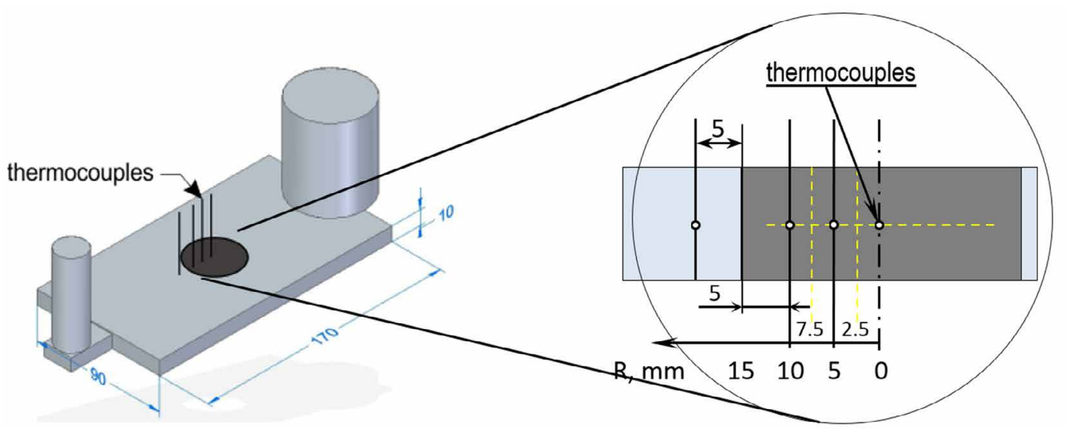

Fig. 2. Pattern of experimental casting

4. RESULTS AND DISCUSSION

The results of temperature measurements are shown in Figure 3.

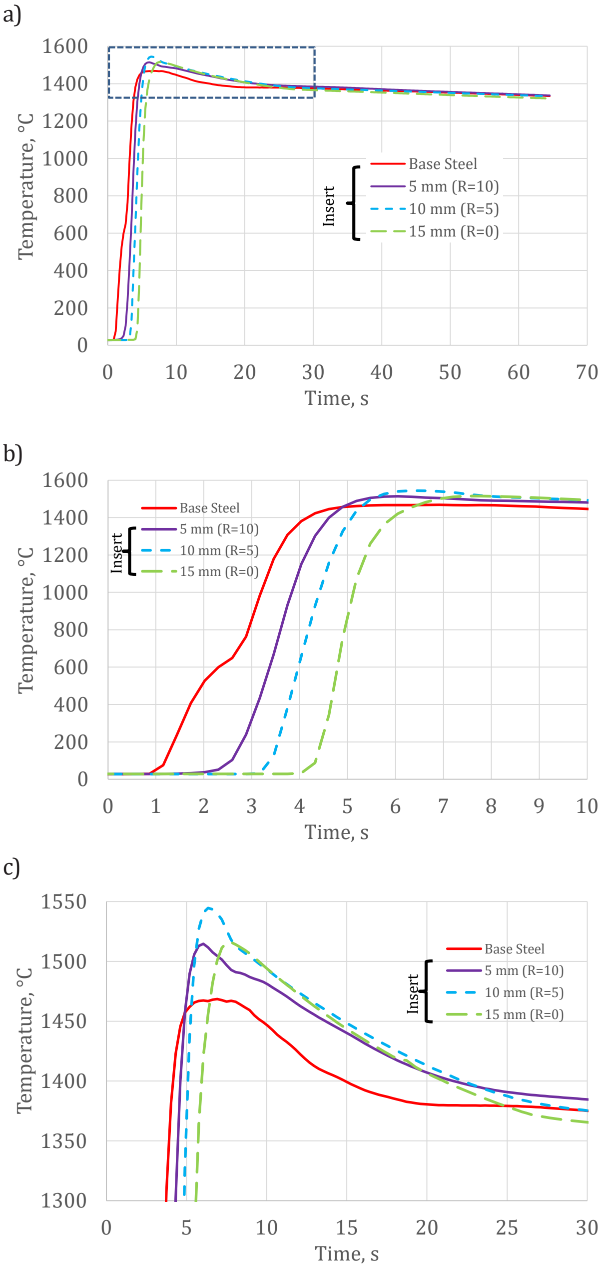

Fig. 3. Temperature changes in the measurement points in the casting and the LCR zone: a) general view; b) temperature increase in the initial period; c) enlargement of the area marked in Figure 3a

Temperature recorded by individual thermocouples rises during the mold filling period. It can be noted that, when the temperature in the liquid steel area exceeds approx. 600°C, the rate of temperature increase in the liquid steel area grows significantly. This is confirmed by the presence of a local minimum on the temperature change rate curve in the base steel area between 2 and 3 seconds of the process (see Fig. 4). This effect can be linked with the fact that the time instant of the exothermic SHS reaction starts in the neighboring compact. It is noteworthy that the relatively low starting temperature of titanium carbide synthesis indicates the very good wettability of components by liquid steel.

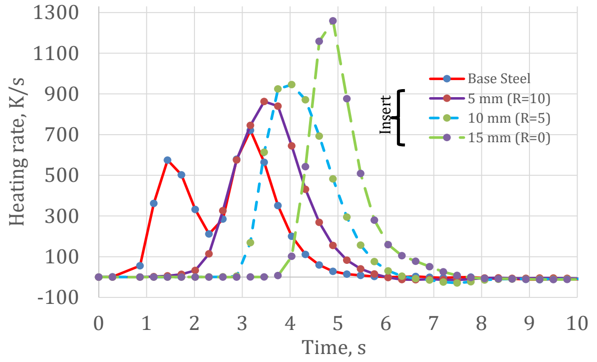

Fig. 4. The rate of temperature changes temperature during mold cavity pouring and SHS reaction of LCR formation in the base casting and in the synthesis zone

The maximum temperature recorded in the area of the synthesis is over 50 K higher than that recorded in the base casting area (Fig. 3c). The difference between the temperature in the LCR zone and in the casting area disappears after about 25–30 s from the start of mold filling (Fig. 3c).

The diagram of temperature gradient change, calculated on the basis of the recorded temperature measurements, is shown in Figure 5. A change of temperature gradient vector sense in point 7.5 mm from the compact center after approximately 5.5 s means that the direction of the heat flux changes from that moment on. If the central part of the compact was initially heated by the steel poured into the mold cavity, and the SHS reaction heat from the outer layer of the compact itself, then from this point of time the temperature in the axis of symmetry of the compact becomes higher, and the central part of the compact is itself cooled through its external layers and the adjacent casting material.

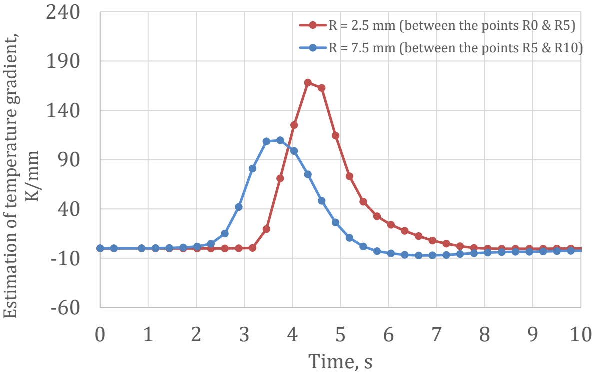

Fig. 5. Evaluation of axial temperature gradient changes in the insert by means of the central difference scheme

The axial symmetry of the compact is taken into account by the calculation of the Laplace operator numerical estimation for the temperature field. The following equation was used in this case:

$$\frac{\partial^2 T}{\partial x^2} \cong \frac{r_2 \,\mathrm{grad}\, T\big|_{r_2} - r_1 \,\mathrm{grad}\, T\big|_{r_1}}{r_2^2 - r_1^2} \qquad (8)$$

The results of this assessment are shown in Figure 6.

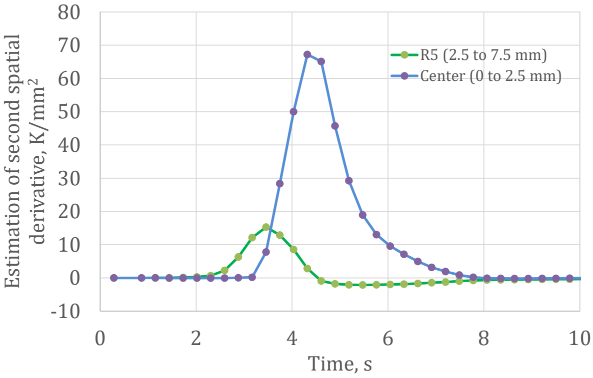

Fig. 6. Laplace operator numerical evaluation for temperature in the insert zone

The measure of the SHS reaction rate $\dot{q}$ is calculated using Equation (3) based on the data presented in Figures 4 and 6. The results of the calculation are presented in Figure 7. The history of the degree of transformation changes calculated from Equation (7) are presented in Figure 8.

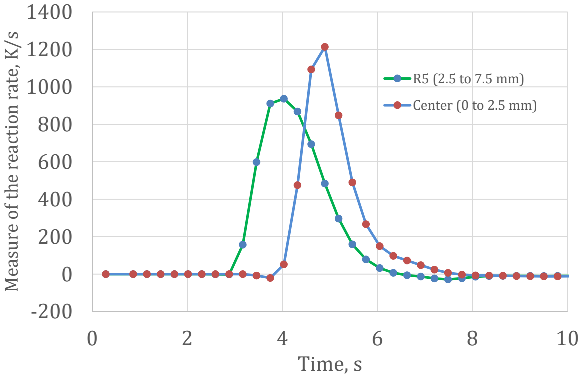

Fig. 7. SHS reaction kinetics of the Ti carbides synthesis in the LCR zone

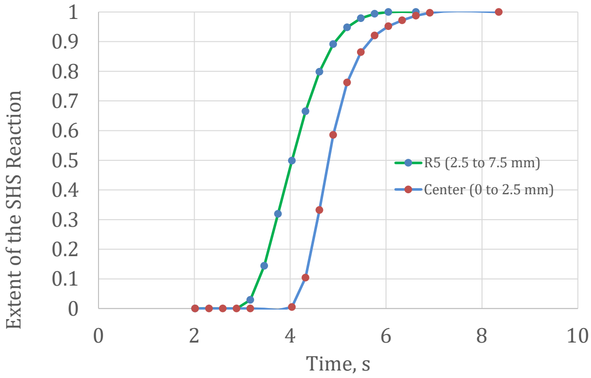

Fig. 8. SHS reaction of TiC completion level in the LCR zone

As it follows from the obtained results, the FTA method may be used for the estimation of the *in situ* SHS exothermic reaction rate in the case of LCR zone formation in the casting. Calculations were performed on the basis of the measurement results for a compact with a cylindrical symmetry 30 mm in diameter prepared from the raw materials for SHS. The estimation results characterize local volumes. In the two cylindrical zones of the compact, the same reaction completion time equal to 3 s was obtained. In the cylindrical layer within radius boundaries of 7.5 to 2.5 mm, the reaction starts at the time instant of 3 s. In the cylindrical zone with a radius of 2.5 mm, the reaction starts 1 s later. These results show that the synthesis rate of titanium carbide in substrates for LCR production is very high. The velocity of the reaction front migration from one of the above volumes to the other is nearly 5 mm/s.

5. CONCLUSIONS

In this paper SHS of titanium carbide in cast steel casting was investigated experimentally and numerically. The following conclusion have been reached:

1. Temperature measurements were carried out in the molded compact prepared from titanium and carbon powders (44 μm) in amount of 50 wt.% and moderator (Hadfield steel) during the filling of the mold cavity and *in situ* SHS reaction of carbide synthesis in the steel casting.
2. The Fourier method of thermal analysis was used to estimate the kinetics of the *in situ* exothermic SHS reaction of carbides synthesis in the two cylindrical volumes of the LCR zone.
3. The time of the SHS *in situ* reaction completion during LCR zone formation in the steel casting, as estimated by the FTA method, is nearly 3 s. The velocity of the synthesis reaction front migration is estimated at 5 mm/s.

REFERENCES

[1] Olejnik E., Szymański Ł., Tokarski T., Opitek B. & Kurtyka P. (2019). Local composite reinforcements of TiC/FeMn type obtained in situ in steel castings. *Archives of Civil and Mechanical Engineering*, 19(4), 997–1005.

[2] Olejnik E., Szymański Ł., Batóg P., Tokarski T. & Kurtyka P. (2020). TiC-FeCr local composite reinforcements obtained in situ in steel casting. *Journal of Materials Processing Technology*, 275(1), 116157.

[3] Olejnik E., Tokarski T., Sikora G., Sobula S., Maziarz W., Szymański Ł. & Grabowska B. (2019). The Effect of Fe Addition on Fragmentation Phenomena, Macrostructure, Microstructure, and Hardness of TiC-Fe Local Reinforcements Fabricated in situ in Steel Casting. *Metallurgical and Materials Transactions A, Physical Metallurgy and Materials*, 50A(2), 975–986.

[4] Sobula S., Olejnik E., Sikora G. & Tokarski T. Strefy kompozytowe uzyskane metodą syntezy in situ w staliwie. Konferencja naukowa „Staliwo – nowe wyzwania przemysłowe", 18–19 April 2013, Kraków.

[5] Ignaszak Z. & Popieralski P. (2003). Właściwości termofizyczne otulin izolacyjno-egzotermicznych oznaczane metodą zagadnień odwrotnych. *Archiwum Odlewnictwa,* 3(9), 209–220.

[6] Ignaszak Z. & Prunier J.-B. (2017). Innovative Laboratory Procedure to Estimate Thermophysical Parameters of Iso-exo Sleeves. *Archives of Foundry Engineering*, 17(1), 67–72.

[7] Fraś E., Kapturkiewicz W., Burbelko A. & Lopez H.F. (1993). A New Concept in Thermal Analysis of Castings. *AFS Transactions*, 101, 505–511.

[8] Fraś E., Kapturkiewicz W., Burbelko A. & Lopez H.F. (1997). Numerical simulation and Fourier thermal analysis of solidification kinetics in high-carbon Fe-C alloys. *Metallurgical and Materials Transactions B*, 28(1), 115–123. Doi: 10.1007/s11663-997-0134-z

[9] Emadi D. & Whiting L.V. (2002). Determination of Solidification Characteristics of Al-Si Alloys by Thermal Analysis. *AFS Transactions,* 110, 285–296.

[10] Gonzalez-Rivera C., Campillo B., Castro M., Herrera M. & Juarez-Islas J.A. (2000). On the Local Microstructural Characteristics Observed in Sand Cast Al-Si Alloys. *Materials Science and Engineering: A*, A279, 149–159.

[11] Gonzalez-Rivera C., Cruz H., Garcia A. & Juarez-Islas J.A. (1999). The Effect of Heat Transfer on Local Solidification Kinetics of Eutectic Al-Si Cast Alloy. *Journal of Materials Engineering and Performance*, 8(1), 103–110.

[12] Djurdjevic M.B., Odanovic Z. & Talijan N. (2011). Characterization of the Solidification Path of AlSi5Cu (l–4 wt.%) Alloys Using Cooling Curve Analysis. *JOM,* 63(11), 51–57.

[13] Moraru L. (2000). Fourier Thermal Analysis of Solidification Kinetics in Molten Aluminium and in Presence of Ultrasonic Field. *Czechoslovak Journal of Physics*, 50(10), 1125–1132.

[14] Piasentini F., Bonollo F. & Tiziani A. (2005). Fourier thermal analysis applied to sodium eutectic modification of an ALSI7 alloy. *Metallurgical Science and Technology*, 23(2), 11–20.

[15] Han Z., Pan H., Li Y., Luo A.A. & Sachdev A.K. (2015). Study on Pressurized Solidification Behavior and Microstructure Characteristics of Squeeze Casting Magnesium Alloy AZ91D. *Metallurgical and Materials Transactions B*, 46(1), 328–336.

[16] Cruz H., Ramirez-Argaez M., Juarez A., Garcia A. & González-Rivera C. (2009). Fourier Thermal Analysis of the Eutectic Formed in Pb-Sn Alloys. *Journal of Materials Engineering and Performance*, 18(5), 441–445.

[17] Baez J.C., Gonzalez C., Chavez M.R., Castro M. & Juarez J. (2004). Fourier Thermal Analysis of the Solidification Kinetics in A356/SiC_p Cast Composites. *Journal of Materials Processing Technology*, 153(SI), 531–536.

[18] Svidro J.T., Dioszegi A. & Toth J. (2014). The Novel Application of Fourier Thermal Analysis in Foundry Technologies. *Journal of Thermal Analysis and Calorimetry*, 115(1), 331–338.

[19] Toth J., Svidro J.T., Dioszegi A. & Stevenson D. (2016). Heat Absorption Capacity and Binder Degradation Characteristics of 3D Printed Cores Investigated by Inverse Fourier Thermal Analysis. *International Journal of Metalcasting*, 10(3), 306–314.

Journal of Casting & Materials Engineering Vol. 4 No. 2 (2020) 29–33
https://doi.org/10.7494/jcme.2020.4.2.29

A Casting Mould for Rapid Tube Hydroforming Prototyping

Andrzej Kochański[*], **Hanna Sadłowska**

Warsaw University of Technology, Faculty of Production Engineering, Narbutta 85, 02-524 Warsaw, Poland
**e-mail: akochans@wip.pw.edu.pl*

Received: 5 May 2020/Accepted: 30 June 2020/ Published online: 17 July 2020
This article is published with open access at AGH University of Science and Technology Press

Abstract

In recent years, hydroforming has clearly expanded its range of industrial applications due to the growing interest in products which combine high strength with low weight. A current limitation of this technology was its economically justified production volume since the costs of producing tools eliminates the possibility of using hydroforming technology in prototype and single part production. The paper presents a freshly patented solution that allows for single part hydroforming. The new technology combines traditional hydroforming machines with a new approach to tool production. The new rapid die is made quickly and cheaply. The use of materials known from the production of foundry moulds causes the die to deform during hydroforming, but it is a controlled deformation. Thanks to the use of numerical modelling, the deformation of the mould cavity is predicted and taken into account at the design stage. The article presents important issues that need to be considered in the design of this innovative process.

Keywords:
hydroforming, casting mould, rapid prototyping, process numerical modelling, hydroforming classification

1. INTRODUCTION

The growing interest in hydroforming as a method of component forming is tightly connected with increased demand to combine the high strength of components with their low weight. This is important in many areas of use, such as aerospace or automotive industries or in the production of bicycle components [1]. In recent years, the development of modern vehicle construction has led to an increase in the application of hydroforming processes in the production of lightweight automotive and aerospace components.

One of the limitations of hydroforming was the fact that the forming is in a short series. A consequence of the high die cost was that hydroforming was only economically justified for a series of 1,000 pieces. The introduction of plastic or even hardwood dies, which are cheaper and easier to prepare, made hydroforming economically justified for shorter series, even for series of 100 pieces [2]. However, the production of individual exemplars still remained economically unjustified.

Rapid changes in machines and devices under production, the necessity for prototyping, as well as individual demand have made it a matter of urgent necessity to develop a new technology which would employ hydroforming but which, at the same time, would make the use of a very cheap forming die possible. In order to reduce the die price to the minimum, dies need to be produced in a very simple way and with the use of common and cheap materials. The development of such a method, as shown in Figure 1, would allow the extension of the hydroforming variety for the entire range of serial sizes of manufactured components.

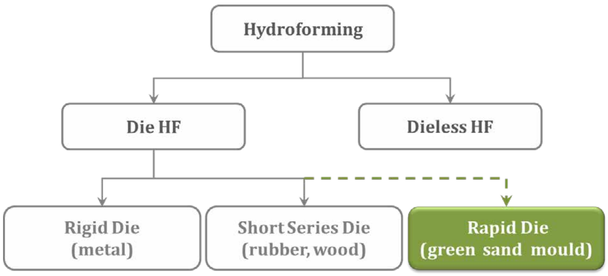

Fig. 1. Process classification according to the tools used in hydroforming

The present freshly patented method for metal tube hydroforming is dedicated to short product series or even single products and prototypes [3]. The method is applicable to forming difficult-to-machine materials. The well-known technique uses dies made of plastic or wood, especially to form short product series. The use of moulding sand and the properly prepared geometry of the casting mould makes it possible to shape materials at high temperatures, something which could not be done in previous short series solutions where a plastic or wooden die were used.

2. RAPID DIE HYDROFORMING TECHNOLOGY

The requirements for cheap and easy-to-obtain materials that may be used in the preparation of prototype hydroforming dies are satisfied by foundry moulding sands, for instance by green sands or by moulding sands with water glass. As originally planned, materials used for foundry moulding sands are cheap, easy to obtain, and in the case of green sands, suitable for reuse. In the process of profile forming, a die made of moulding materials gives in to pressure and does not stick to the stable, unchanging shape of the die cavity. The main point of the proposed technological solution is to set the original shape of the die cavity in the function of the properties of the moulding sand used for the making of the die, as well as the properties of the profile under forming. The original shape of the die cavity is selected in numerical modelling.

Figure 2 schematically represents the forming mechanism proposed in the PL424401 patent [3]. The expanding profile in the die cavity increases its volume and thereby displaces the moulding sand which induce its quick local compacting. The moulding sand is compacted in places of contact with the profile, which inhibits and eventually stops the profile extension process. At the same time, the areas of the profile unsupported or partially supported by the mould undergoes free forming. The locking expansion in selected areas with the simultaneous free or semi-free shaping in other areas of moulding die enables to achieve the designed shape.

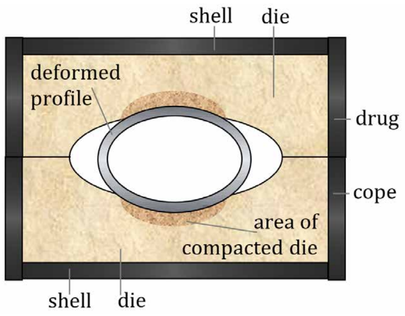

Fig. 2. A cross-section of the die together with the profile under forming – the schematic forming mechanism (based on the original patent [3])

The first step in developing the RTH technology based on the RTH method proposed in the patent was to build a numerical model aimed to investigate the influence of moulding sand properties on the tube deformation method in the new technological process. Such an approach seems to be convenient to estimate the outcome of and for controlling the process of deforming the moulding die which takes place during the profile expansion, as well as for establishing the ultimate shape of the profile. The profile shape depends on the properties of the material from which the profile is made, its original geometry, as well as the properties of the moulding sand from which the die has been made and the boundary conditions (for instance, the friction between the moulding sand and the profile under forming).

As has been demonstrated, for instance, in [4], it is the Mohr–Coulomb (M-C) material model which is commonly used for the initial calculations in the numerical modelling of moulding sands in the compacting process. For moulding sands and loose materials, the cohesion coefficient c and the internal friction angle ϕ, which are the critical values for the M-C model, assume the values within the following ranges: $c = 0.1–5.0$ MPa, and $\phi = 10°–50°$ [5]. Both parameters determine the internal resistance of the material related to tangential stress caused by normal pressure [6]. From a literature review on moulding sands, it emerges that a change of cohesion and internal friction angle makes it possible to exert a considerable influence on the way in which the profile is being formed. However, the authors of this article wanted to check the real impact of mass parameters on the deformability of tubes in RTH processes. The research provides for determining the impact of both moulding sand parameters (c and ϕ) on the tube deformability in the RTH process. Therefore, a number of numerical experiments were performed using a variety of parameters c and ϕ combinations using FEM simulations of RTH process of the example presented in the patent document. All of the examined combinations of cohesion c and friction angle ϕ are shown in Table 1. The symmetry of the moulding die-profile system was used and the quarter section was modelled to simplify and speed up the calculations. A geometric model of the Plane Strain type was used, in which 2D triangular elements and quadrangular 2D elements were used to generate the mesh covering the moulding die and tube respectively, see Figure 3. In the zone of initial contact between the mass and the tube, the mesh was compacted.

The mass was limited from the outside with rigid elements intended to simulate a moulding box which prevents the mass from moving outwards. Pressure was applied to the inner edges of the tube elements and the value pressure increased from 0 MPa to 420 MPa. The simulation time was set at 5 seconds and divided into 100 equal increments.

Table 1
Numerical calculations cases in c and ϕ analysis

Cohesion c [MPa]	Internal friction angle ϕ [°] 10	20	30	40	50
0.1	1	2	3	4	5
0.5	6	7	8	9	10
1.0	11	12	13	14	15
1.5	16	17	18	19	20
5.0	21	22	23	24	25

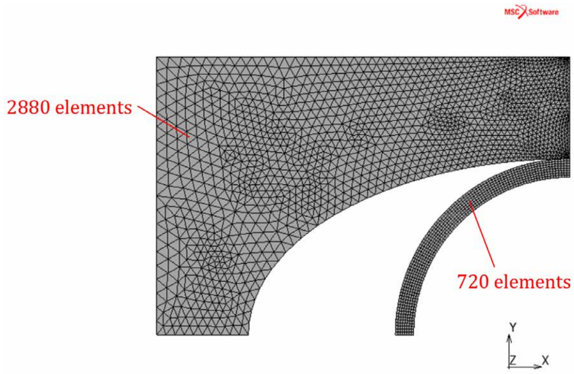

Fig. 3. A mesh in RTH numerical model

Classic green sand (with bentonite) masses take values from $c = 0.1$ and $\phi = 10$ while high values of c and ϕ e.g. 5 and 50, are characteristic for soils e.g. sand rocks [7]. Moulding sands with inorganic binders are characterized by lower parameters, not greater than $c = 1.5$ and $\phi = 40$. Such a significant c and ϕ dispersion causes that masses with bentonite and masses with water glass binders will behave significantly differently during profile expansion. The numerical simulations results confirmed the clear difference in behaviour, as shown in the two extreme cases 1 and 19 of numerical modelling (both marked in grey in Table 1). These two distant range cases were selected to effectively illustrate the impact of cohesion and friction angle parameters. The case 1 refers to the low internal resistance ($c = 0.1$ MPa, and $\phi = 10°$) and case 19 refers to the high internal resistance ($c = 1.5$ MPa, and $\phi = 40°$).

The calculations of the results of the deformation of the die and the tube for 1 and 19 cases are presented in Figure 4. The colours used in the pictures represent the displacement moulding sand of the die in the same process time and internal profile pressure load (420 MPa). The case 1 results (Fig. 4a) show considerably larger moulding sand displacement caused by the movement of the expanding profile. At the same time, a much larger deformation of the tube in the contact zone with the die can be observed than in the case of using a mass characterized by a much greater internal shear resistance, i.e. for case 19 shown in Figure 4b.

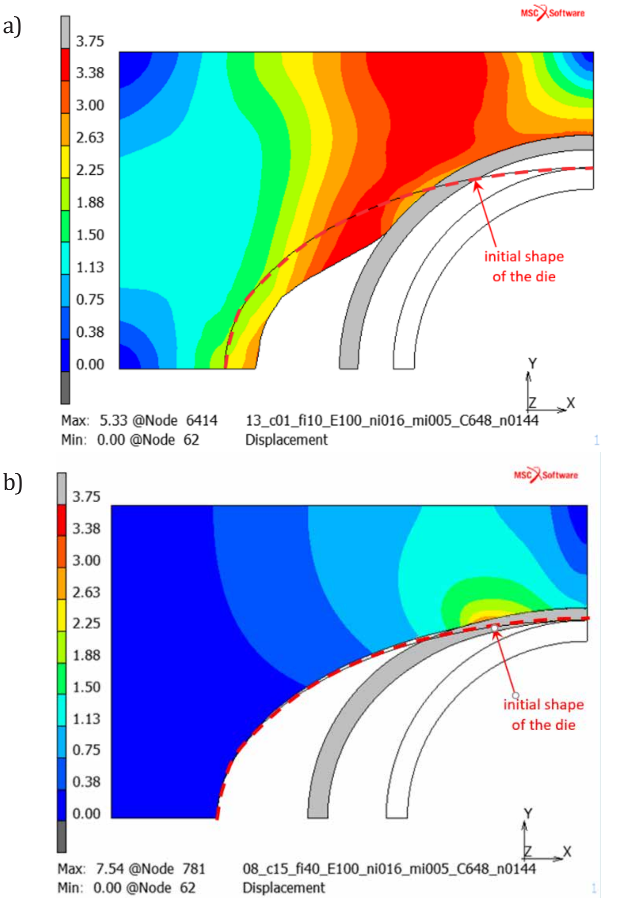

Fig. 4. Mass displacement (in millimetres) during profile hydroforming with an elliptical cross-section die cavity in two kinds of moulding sand properties: a) $c = 0.1$ and $\phi = 10°$; b) $c = 1.5$, $\phi = 40°$

From the comparison presented in Figure 4 one can also observe a significant difference in the deformation of the profile in the directions of the major and minor axes expressed in the proportion of the large axis and the small axis. For case 1, the axes ratio is equal to 1.08, while for case 19 it is 1.34. Furthermore it is worth noting the behaviour of the moulding sand during the forming process. The occurrence of mass compaction associated with tube expansion is easily discerned in the case of mass with c and ϕ high values (Fig. 4b) where the outline of the moulding die cavity moves entirely over the initial shape of the die during the expansion process. This clearly indicates the reduction of the mass volume, i.e. the compaction of the mass. However, for mass with lower ϕ and c, two processes occur simultaneously: mass compaction and displacement into areas not supported by a hydroformed profile. The part of the moulding sand visible in Figure 4a moved below the initial shape and which indicates that only part of the mass has been compacted but some of it just displaced.

3. METHODS AND MATERIALS

Experimental studies were conducted with the use of the tube hydroforming measurement site (TH stand), designed and built at the Warsaw University of Technology hydroforming stand HF at the Department of Metal Forming and Foundry [8]. The TH stand allows both die and free tube hydroforming processes to be performed, thereby making it possible to obtain information about the material, as well as optimal process parameters [9] and makes useful to examine the new RTH method.

A methodology of RTH was developed to adjust and perform the first experiments on the TH stand and the special geometry of the die has been designed to put into practice the main idea of the RTH method.

The original shape of the die followed from the assumption that the profile under forming would be in contact with the moulding mass from the very beginning – thus, the original cavity diameter equalled the outside diameter of the profile under forming. However, it turned out that the friction force following from the moulding sand-profile friction coefficient is so big that it hinders the displacement of the profile material along the axis, thereby making impossible the feeding of the profile under forming in its thinned areas. A photo of the moulding die and the initial profile geometry are shown in Figure 5 and Figure 6, respectively.

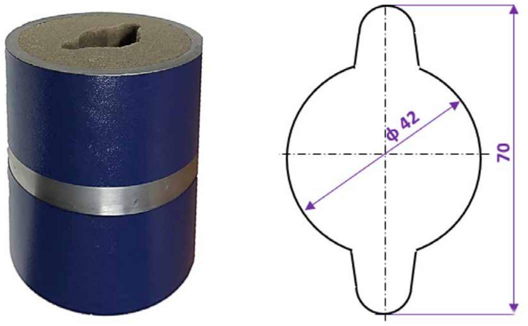

Fig. 5. A die made of moulding sand and the die cavity geometry

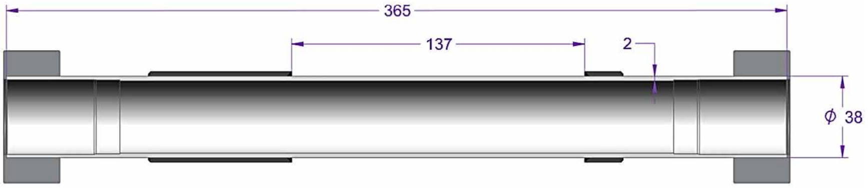

Fig. 6. The initial profile geometry – RTH tube specimen: outer dimension Ø38; thickness of the wall 2 seamless tube (material: normalized steel E235)

In the initial experimental studies, moulding sand with water glass was used. The composition of the moulding sand is presented in Table 2 that also shows the relative percentages traditionally used to report the composition of the mass containing the binding material and the catalyst.

Table 2
The composition of the moulding sand with water glass

Moulding sand component	Percentage	Relative percentage
Sand: Grudzeń Las 0.32/0.40/0.20	92.6	100 sand matrix
Sodium water glass R-145	6.5	7 relative to sand matrix
Ester hardener (of ethylene glycol diacetate) Flodur FM-4	0.9	14 relative to water glass

Preparation of the moulding sand included pre-mixing the sand matrix and water glass R-145 in a Mix-Muller Batch Mixer for 5 minutes, followed by further mixing for 1 minute with ester hardener. Standard specimens were made out of the prepared moulding sand for compressive strength tests (a cylindrical specimen Ø = 50 mm, h = 50 mm). The specimens were made in the laboratory rammer LUA-2e. Three hours after forming the moulding sand exhibited the mean compressive strength of R_m = 2 MPa, and after 5 days R_m = 5 MPa. The die was made out of the prepared moulding sand. The die mounted on the experimental stand is presented in Figure 7.

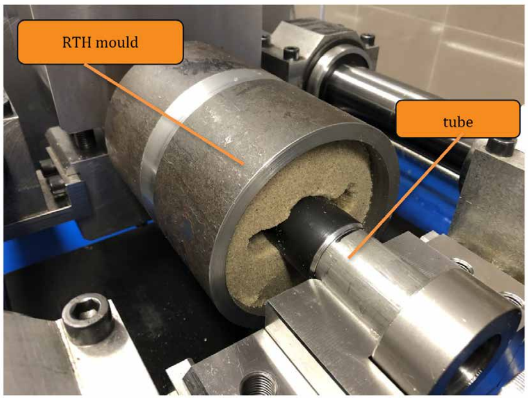

Fig. 7. The test stand with the installed die made of moulding sand with water glass

4. EXPERIMENTAL RESULTS

In the case of the alternative geometry, contact between the moulding sand and the profile occurred at a later stage of forming, which made considerable profile deformation possible. Figure 8a shows the profile subjected to forming in the type B die, while Figure 8b represents the profile obtained as a result of forming, as well the cross-section geometry in the central part of the profile under forming.

The obtained profile shape clearly demonstrates the influence of the die cavity geometry on the profile under forming. In the process of forming, profile deformation was limited in the area of contact between the profile and the moulding sand, and at the same time the deformation was considerably larger in the area with no contact between the profile and the die cavity. As a result of forming, a profile with the initial circular cross-section of the 38 mm diameter, what was obtained was a profile with the elliptical cross-section with the major axes of 43 mm and 53 mm.

As demonstrated in the numerical modelling (Fig. 4a, b), the properties of the moulding sand exert a decisive influence on the area of contact between the profile under forming and the die cavity.

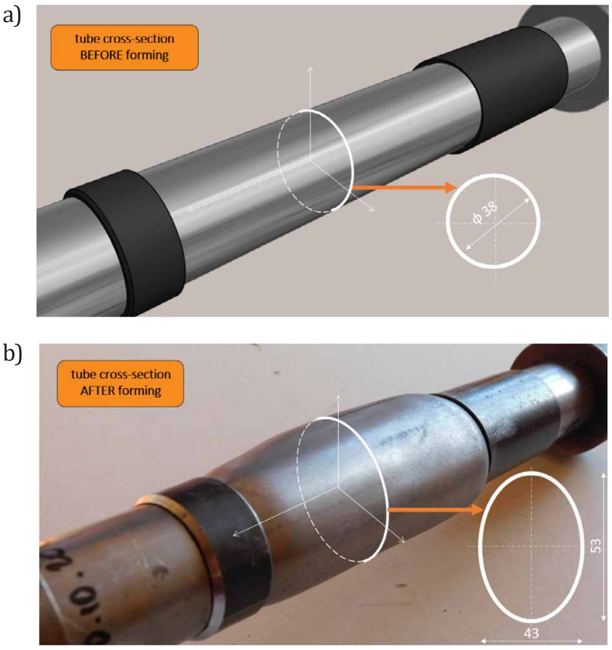

Fig. 8. The dimensions of the cross section of the profile under forming: a) initial geometry – diameter Ø38 mm; b) after forming – elliptical cross-section

5. SUMMARY

The initial experimental tests demonstrated the viability of the proposed new method for obtaining diverse profile shapes, including profiles with an elliptical cross-section involving a considerable difference between the two diameters. Numerical modelling demonstrated a considerable influence on the profile under forming of such moulding sand parameters as the cohesion coefficient c or the internal friction angle ϕ.

The possibility of obtaining considerable deformations is directly dependent on the profile material's capability of being displaced into the deformation area. It is worth noting that the stability of the process requires the development of mould compacting methods in the entire volume and it is an important factor in obtaining a commercially repeatable profile shape.

REFERENCES

[1] Kocańda A. & Sadłowska H. (2008). Automotive component development by means of hydroforming: A review. *Archives of Civil and Mechanical Engineering*, 8(3), 55–72. Doi: 10.1016/S1644-9665(12)60163-0.

[2] Pinto M., Santos A., Teixeira P. & Bolt P. (2008). Study on the usability and robustness of polymer and wood materials for tooling in sheet metal forming. *Journal of Materials Processing Technology*, 202(1–3), 47–53. Doi: 10.1016/j.jmatprotec.2007.08.082.

[3] Kochański A. & Sadłowska H. (2019). Patent no. PL424401. Sposób hydromechanicznego kształtowania profili cienkościennych i matryca do hydromechanicznego kształtowania profili cienkościennych. Biuletyn Urzędu Patentowego, Urząd Patentowy Rzeczypospolitej Polskiej. Wynalazki i Wzory Użytkowe, 17, 11.

[4] Bast J., Kadauw A. & Malaschkin A. (2009). Optimising of Moulding Parameters for Green Sand Compaction by Computer Simulation and a New Compaction Measuring Device. *International Journal of Metalcasting*, 3(2), 55–65.

[5] Waszkiewicz S. (1992). Wpływ błędów odwzorowania wnęki formy na dokładność wymiarową odlewów. *Prace Naukowe – Politechnika Warszawska. Mechanika*, z. 147. Warszawa: Wydawnictwa Politechniki Warszawskiej.

[6] Dodge Woodson R. (2011). *Appendix III – Foundry Sand Facts for Civil Engineers*. In: Concrete Portable Handbook. Elsevier, 299–372.

[7] Godula T. (1984). *Metoda rozpoznawania warunków geologiczno-inżynierskich warstw karbońskich dla potrzeb projektowania kopalń oraz wyniki jej zastosowania w rejonie Bzie-Zebrzydowice* [Doctoral Thesis]. Gliwice: Politechnika Śląska.

[8] Sadłowska H. (2016). Strains in free tube hydroforming process. *Journal of Manufacturing Technologies*, 41(1), 7–11.

[9] Sadłowska H., Jasiński C. & Morawiński Ł. (2020). Strain measurements on the tube hydroforming testing machine. *Archives of Metals and Metallurgy*, 65(1), 257–263.

Journal of Casting & Materials Engineering Vol. 4 No. 2 (2020) 34–40
https://doi.org/10.7494/jcme.2020.4.2.34

Microstructural Analysis of Concrete Using Cow Bone Ash for Alkali-Silica Reaction (ASR) Suppression

Ariyo Adanikin[a,b*], **Funsho Falade**[a], **Adewale Olutaiwo**[a]

[a]Department of Civil and Environmental Engineering, University of Lagos, Akoka, Nigeria
[b]Department of Civil Engineering, Elizade University, Ilara Mokin, Ondo State, Nigeria
e-mail: nukee02@gmail.com

Received: 21 April 2020/Accepted: 1 July 2020/ Published online: 17 July 2020
This article is published with open access at AGH University of Science and Technology Press

Abstract

Concrete pavements are prone to microstructural changes and deterioration when exposed to Alkali-Silica Reaction (ASR). ASR results in strength reduction, cracking, spalling and other defects in the concrete if left unchecked. Supplementary Cementitious Materials (SCMs) such as Cow Bone Ash (CBA) however can be used to improve concrete performance, hence its use in this study. Concrete samples were prepared at replacement levels of 0%, 5%, 10%, 15%, 20% and 30% of cement with Cow Bone Ash. The concrete samples were then subjected to petrographic and Scanning Electron Microscopy (SEM) analysis. Petrographic examination shows that the minimal and least amount of ASR gels and micro cracking were observed at 15% CBA replacement of cement in the concrete samples. Scanning Electron Microscopy (SEM) analysis shows that changes in the elemental composition of the concrete samples is related to the effect of CBA which enhances adhesion in the concrete. SEM analysis show that, in general, the change in microstructure in the concrete was mainly due to the change in the arrangement of the C-H-S compounds. The microstructure analysis indicates that CBA in concrete influences the densification of the concrete at the transition zone, resulting in a much lower porosity. This results in the concrete having a tightly bound layer that repels ingress of water and thereby inhibiting cracks and gel formation as water is a contributing factor to the ASR in concrete.

Keywords:

petrographic analysis, Scanning Electron Microscopy, Cow Bone Ash, Alkali-Silica Reaction, concrete pavement

1. INTRODUCTION

Alkali-silica reactivity has been recognized as a potential source of distress in concrete since the late 1930s because in hardened concrete, aggregates containing reactive silica interact with alkali (sodium oxide and potassium oxide) present in the cement to form expansive alkali silicate gels which disrupt the concrete and thereby forming pattern cracks. The Alkali-Silica Reaction is a type of an internal concrete deterioration which occurs within its entire volume and ASR negative effects are observed in elements such as concrete pavements [1]. ASR produces gels which causes concrete swelling and deterioration when it is exposed to temperature, loadings and humidity. Concrete used in rigid pavements when they deteriorate, compromise the durability and good functioning of the pavements. Sharma [2] found that the osmotic pressure due to alkali-aggregate reaction that occurs on the set cement gel is responsible for concrete defects. The Alkali-Silica Reaction, if unchecked, may cause other problems like pop-outs, spalling etc. and concrete slab may require partial-depth or full-depth repair depending on severity. Factors that promote alkali-aggregate reactions needs to be controlled to keep the pavement away from the ASR menace. If any of these factors are partially or completely removed, ASR will be reduced or will not take place [3]. Hence the use of non-reactive aggregates, low alkali cement and pozzolanas can help in this regard. Alkali-Silica Reaction is a serious problem in concrete when related to rigid pavements considering that once it occurs, no repair methods are available to efficiently and definitely stop the process of ASR and associated damage. Therefore, the best approach is to mitigate it from the onset.

Alkali-Silica Reaction has also been identified on many rigid pavements in the United States of America as seen in its commercial airports Portland Cement Concrete (PCC) pavements in places such as Denver and Colorado Springs in Colorado;

Hartsfield-Jackson Atlanta International Airport, Georgia. More recently, ASR was identified at the Detroit Metropolitan Airport [4]. Because of the ASR severity, Runway 4L-22R will need to be replaced. Northwest Arkansas Regional Airport (XNA) is in the process of replacing their current 16/34 runway due to ASR. It will cost approximately $75 million to construct a temporary runway and reconstruct the 16/34 runway. The runway was constructed in 1998, but has experienced significant distress due to ASR. Distress was manifested through significant slab panel expansion, joint misalignment, heaving, and joint closure. A bridge in Finland required demolition and replacement owing to ASR damage [5]. Also, the concrete containment structures of nuclear power plants in Canada which were designed as crack-free structures by applying biaxial pre-stressing have been damaged due to ASR [6]. Alkali-Silica Reaction has caused problems in at least 46 countries thus, making ASR a serious worldwide problem [7].

Disposal of wastes resulting from myriads of human activities continues to be a problem especially in developing nations, where effective and efficient wastes disposal system is lacking. In the third world countries, the most common and readily available material that can be used to partially replace cement without economic implications are agro and industrial based wastes. These industrial and agricultural wastes are also becoming a health and environmental problem especially in the developing nations where technology for efficient waste disposal is lacking. One such waste product, whose generation runs to millions of tons in Nigeria, are cow bones, from which pulverized bone is obtained [8]. The present disposal system of burning in open sites and indiscriminate dumping on any site does not augur well for the health of human beings and it constitutes environmental hazard.

Supplementary Cementitious Materials (SCMs) such as CBA can be used to improve concrete performance (workability, durability and strength) in its fresh and hardened state as they contribute to the properties of the concrete through hydraulic or pozzolanic activity [9]. Hassan [10] stated that both silica fume and fly ash admixture provide additional benefits to the microstructure homogeneity of hydrated cement paste in concrete. Additionally, the spherical shape of the fly ash and silica fume grains helps to improve the microstructure of cement paste particularly in the Interfacial Transition Zone (ITZ) thereby their importance in concrete as this aids the reduction of ASR gel and crack production. Sarah and Magudeswaran [11] in their study revealed that based on the comparison of the microstructure of concrete mixes, it is clear that the hydration process in the mixes with supplementary materials was different from conventional concrete mix. This was due to the development of C-S-H gel in mixtures with supplementary materials, which is lower than the standard concrete mixture. Investigations by [12] through the Scanning Electron Microscopy (SEM) method shows that ternary blended concrete mix of 70% of ordinary Portland cement, 20% of metakaolin and 10% of microsilica is good for use as a fire resistant structural material. The pozzolanic materials combination when analyzed using SEM showed increasing adhesion and compressive strength hence their ability to inhibit gel and crack formation in the concrete on exposure to fire.

SEM analysis by [13] shows that the dense microstructure of concrete admixed with pozzolanic materials leads to increasing compressive strength of the concrete. Increasing compressive strength of concrete will inhibit the activities of ASR in concrete pavements. Uzbas and Aydin [14] investigated use of fly ash in concrete with Scanning Electron Microscopy and x-ray diffraction. The study revealed that fly ash delivers great performance in concrete because a large amount of silica exists in it and it shows strong pozzolanic property that reaches high strength and increases the durability of concrete. The SEM analysis showed that the usage of fly ash decreases gaps and increases C-S-H which is also a hydration production. When Portland cement was replaced with 10% fly ash by weight, the microstructure and compressive strength of the concrete improved.

To reduce ASR potential requires understanding the ASR mechanism; properly using tests to identify potentially reactive aggregates; and, if needed, taking steps to minimize the potential for expansion and related cracking using Cow Bone Ash (hereafter, CBA) which this study provides a great insight and understanding to.

2. DESCRIPTION OF THE RESEARCH

The concrete mix was designed according to Road Note 4 method of the Department of Scientific and Industrial Research. Natural fine aggregate (sand), cement, CBA aggregates were used. Six different mixes (M1, M2, M3, M4, M5, M6) were prepared at replacement levels of 0%, 5%, 10%, 15%, 20% and 30% of cement by Cow Bone Ash in the concrete samples. 18 thin sections (3 thin sections from each of the concrete mix samples) were produced in total. Each concrete mix sample was cut using a cutting machine to a square shape of 25 mm × 25 mm × 5 mm dimensions. The concrete thin section samples were then subjected to petrographic and Scanning Electron Microscopy (SEM) analysis and interpreting the data obtained in light of the study.

Petrographic and Scanning Electron Microscopy (SEM) Analysis

Petrographic analysis relies on a computer image analysis program designed to quantify the degree of microcracking and the amount of silica gel resulting from ASR. Petrographic analysis helps to identify the nature of deterioration or defects, to determine the degree of damage and to evaluate whether the damage will continue in a concrete sample. Petrographic analysis results are achieved by measuring microcracking, air void structure, aggregate deterioration, and any other possible modes of concrete deterioration due to ASR that are relevant for service life estimation of a rigid road pavement. For the petrographic analysis, the specimens were lessened using an emery cloth and carborundum powder to a thin sheet measured by a micrometer screw gauge to a thickness of about 0.04 mm. The specimens were covered and left for 24 hours after which they were washed, cleaned with spirit, and later with water. Using the Greggory Bottley

Reflected Light Polarizing microscope, the thin sections slides were then subjected to microscopic examinations. This test was carried out to align with BS 1881-211 [15].

Scanning Electron Microscopy analysis is used to identify and photograph submicroscopic features, and/or determine causes of failure in concrete that may be due to the effect of ASR. It provides information on primary and secondary mineral phases in paste, pores, cracks and micro cavities, morphology of phases, source and deposition area for the mineral phases, identity of tiny micron size mineral phases not visible in the optical microscope. In addition, the SEM analysis gives details on chemical composition of mineral phases, chemical zoning or variation through crystals and through the entire material which are all vital in assessing the effects of the CBA on ASR in the concrete mixes. For the SEM analysis, the specimens (25 mm × 25 mm × 5 mm) were polished with silicon carbide using a rotating grinder and mounted against a 25 mm diameter glass plate with epoxy. The samples were cut 2–3 mm thick by using a diamond slicing wheel with propylene glycol coolant being a lubricant to make both sides of the specimen parallel to one another. The specimens were then scooped and polished with silicon carbide using a wheel grinder. Further polishing was conducted on a glass plate with aluminum powder. Post polishing, the specimens were soaked in acetone and placed in an ultrasonic bath. The specimens were then examined using a JEOL JSM-35CF SEM-EDX in the backscatter mode. This test was carried out to align with ASTM C1723 [16].

3. RESEARCH RESULTS AND ANALYSIS

3.1. Petrographic Analysis

The computer image obtained from the study is as shown in Figures 1–6. The images illustrate the effects of ASR on concrete in a rigid pavement as viewed from prepared thin section slides on the microscope at magnifications ranging from 40 m to 100 m.

Figure 1 shows petrographic images of the concrete samples at 0% CBA replacement. High level of gel and crack formation observed. Figure 2 shows petrographic images of the concrete samples at 5% CBA replacement. ASR gel and bubbles are very visible within the concrete samples. Figure 3 shows petrographic images of the concrete samples at 10% CBA replacement. Reduced crack levels compared with 0% and 10% CBA observed. Microcracking lines also observed within the concrete sample. Figure 4 shows petrographic images of the concrete samples at 15% CBA replacement. Minimal and least amount of ASR gels and micro cracking were observed. These results can be related to flocculation and discontinuation of gel production that occurs at 15% CBA production as the CBA has sealed up the cracks and inhibited gel production. Figure 5 shows petrographic images of the concrete samples at 20% CBA replacement. Increase in gel production observed compared to 15% CBA addition. Figure 6 shows petrographic images of the concrete samples at 30% CBA replacement. ASR gel bubbles visible on concrete sample with limited microcracks.

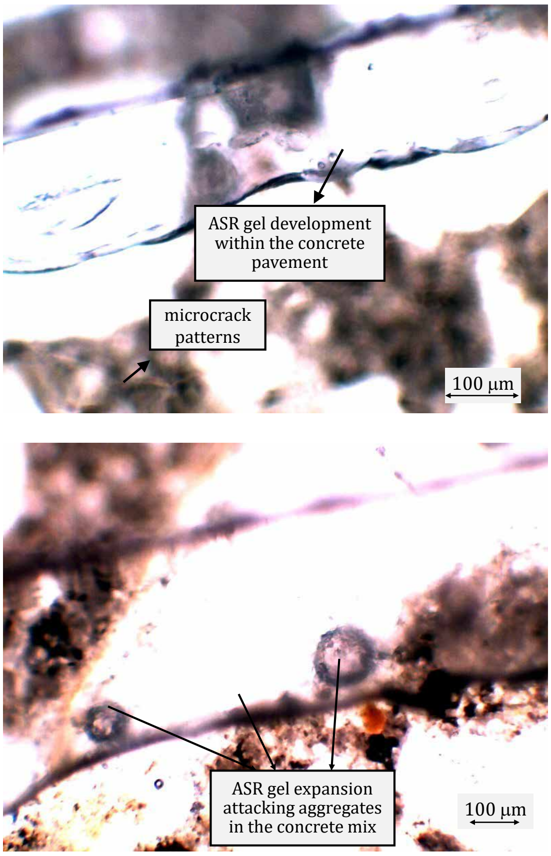

Fig. 1. Petrographic images at 0% CBA replacement

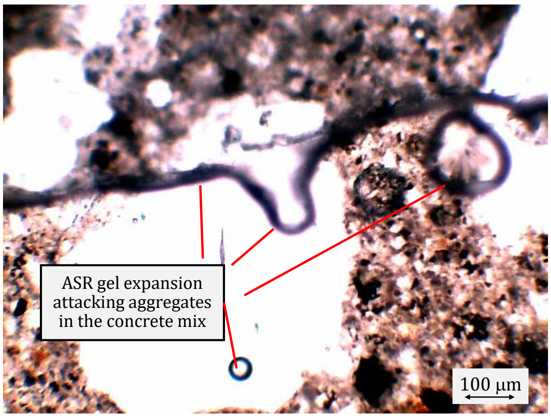

Fig. 2. Petrographic images at 5% CBA replacement

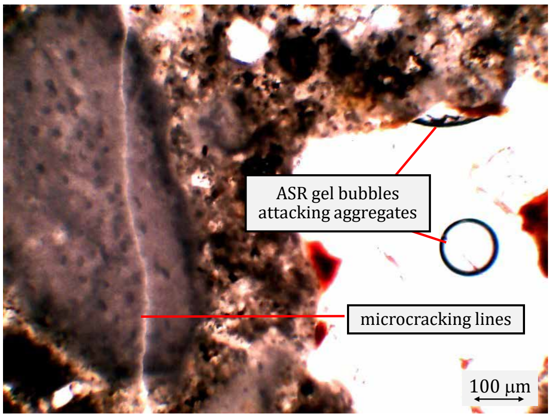

Fig. 3. Petrographic images at 10% CBA replacement

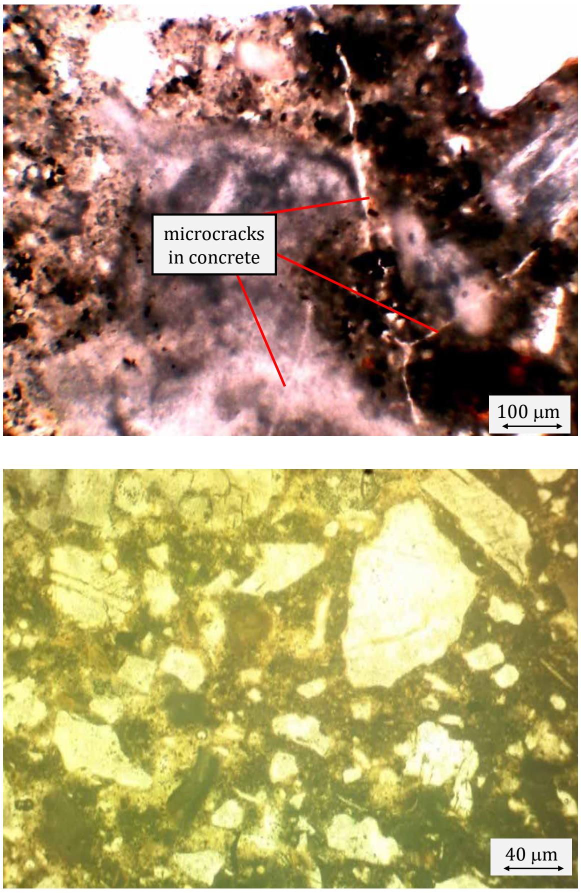

Fig. 4. Petrographic images at 15% CBA replacement

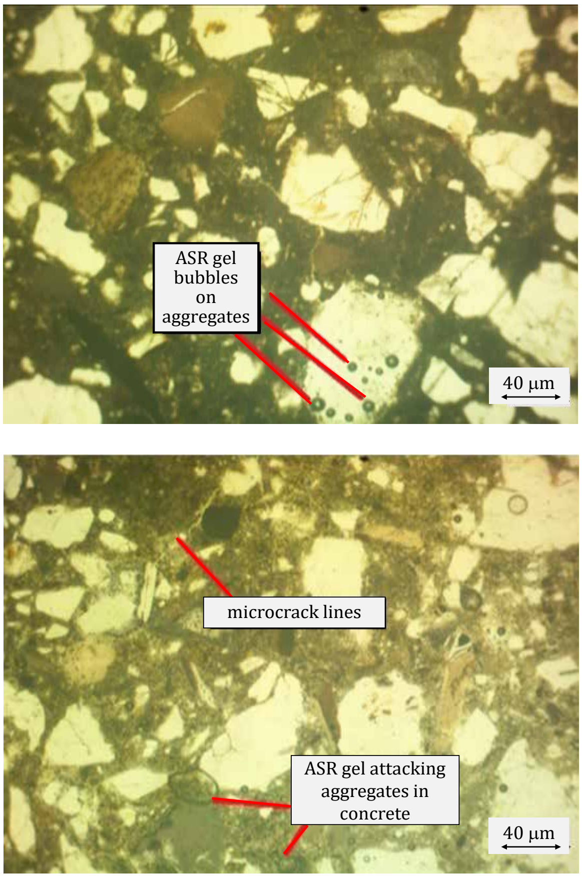

Fig. 5. Petrographic images at 20% CBA replacement

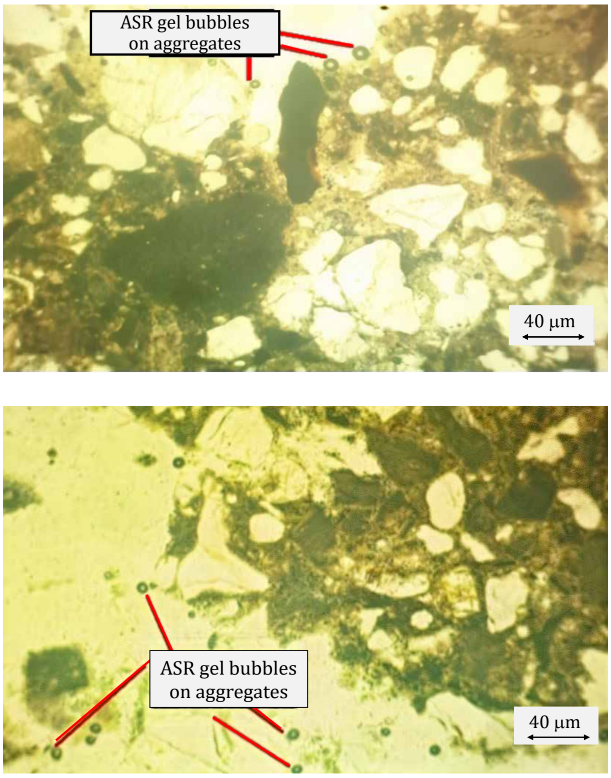

Fig. 6. Petrographic images at 30% CBA replacement

3.2. Scanning Electron Microscopy (SEM) Test

The Backscatter Electron Detector (BSD) and Energy Dispersive X-ray Spectroscopy (EDX) method of Scanning Electron Microscopy (SEM) of the cement-CBA concrete samples were imaged using a focused electron beam that is rastered across the samples surface. This was done to elastically detect scattered electrons that affects the elemental and microstructural characteristics of the concrete samples.

As shown in the Figures 7–12, high levels of calcium content by weight was observed in the concrete samples. The calcium content has a strong impact on the concrete's strength, workability and setting time. The calcium content also strongly impacts the early strength gained by the concrete sample with 0% CBA. According to [17] the high carbon content in the concrete samples helps to decrease drying shrinkage and increases flexural toughness of concrete samples. Liu et al. [18] also stated that high carbon content in concrete enhances its compressive strength and resistance to cracking. Oxygen is also a prominent element in the concrete samples. This is in consonance with [19] that oxygen is an important binder in concrete structures and without it, rigidity of structures will be compromised. This have affected the properties of the concrete in several ways. Silicon percentages in the concrete samples also varies and plays a prominent role in the concrete's properties as it affects the concrete strength, durability, reduces water absorption capacity and helps it to resist chloride ion penetration [20]. Several other elements exist in the concrete samples at varying atomic concentrations and weight concentrations as shown by the SEM analysis results in Figures 7–12.

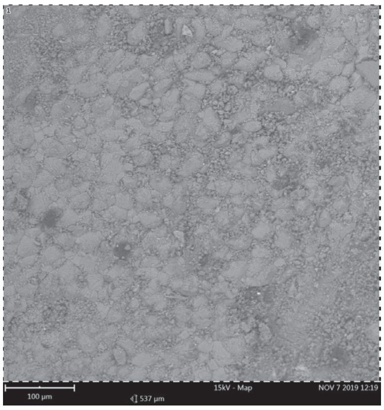

Element symbol	Atomic conc. [%]	Weight conc. [g]
Ca	46.91	66.57
C	26.42	11.24
O	13.36	7.57
Si	6.37	6.34
Al	2.98	2.85
Fe	1.19	2.35
P	0.86	0.94
K	0.42	0.58
S	0.51	0.57
Mg	0.50	0.43
Ti	0.18	0.30
Na	0.32	0.26

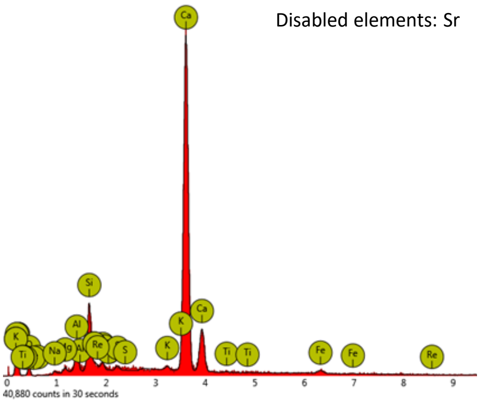

Fig. 7. SEM analysis result at 0% CBA

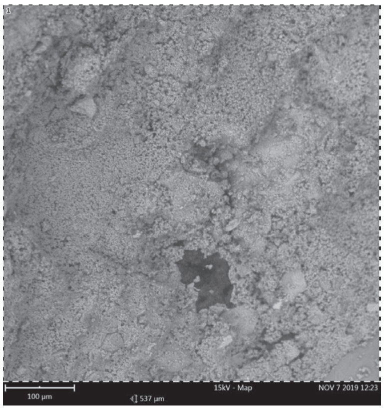

Element symbol	Atomic conc. [%]	Weight conc. [g]
Ca	54.05	68.79
Si	11.17	9.97
C	15.93	6.08
O	10.16	5.16
Fe	1.85	3.29
P	2.07	2.04
Al	2.03	1.74
S	1.18	1.20
Ti	0.51	0.78
Mg	0.57	0.44
K	0.33	0.41
Na	0.14	0.10

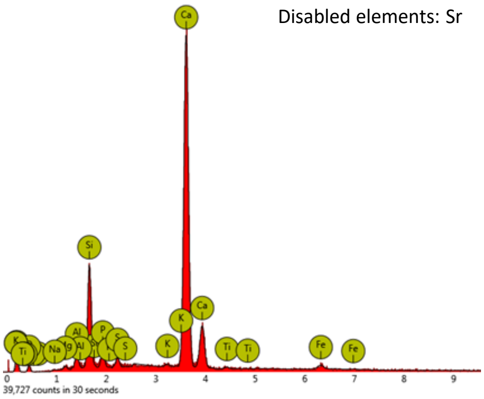

Fig. 8. SEM analysis result at 5% CBA

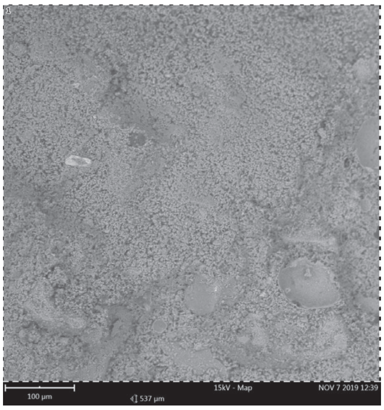

Element symbol	Atomic conc. [%]	Weight conc. [g]
Ca	53.24	67.85
Si	8.43	7.52
C	17.10	6.53
O	9.19	4.68
Fe	1.95	3.47
S	2.54	2.59
Al	2.52	2.16
P	2.07	2.04
K	1.02	1.27
Cl	0.76	0.86
Mg	0.76	0.58
Ti	0.18	0.27
Na	0.25	0.19

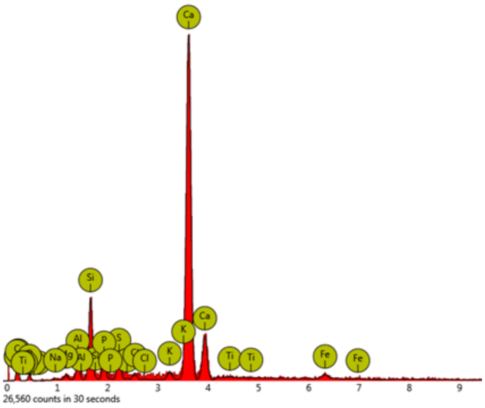

Fig. 9. SEM analysis result at 10% CBA

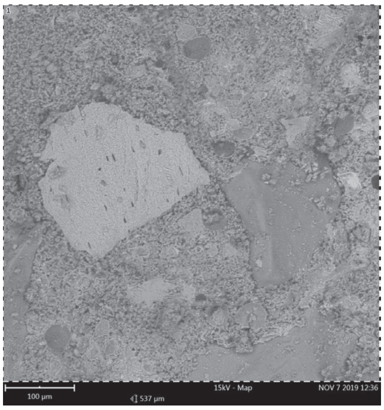

Element symbol	Atomic conc. [%]	Weight conc. [g]
Ca	43.66	59.20
Si	12.82	12.18
C	21.25	8.63
O	11.73	6.35
P	3.86	4.04
Zr	0.81	2.51
Fe	1.28	2.42
Al	1.90	1.74
S	1.58	1.72
Ti	0.31	0.51
Mg	0.53	0.43
K	0.12	0.16
Na	0.15	0.12

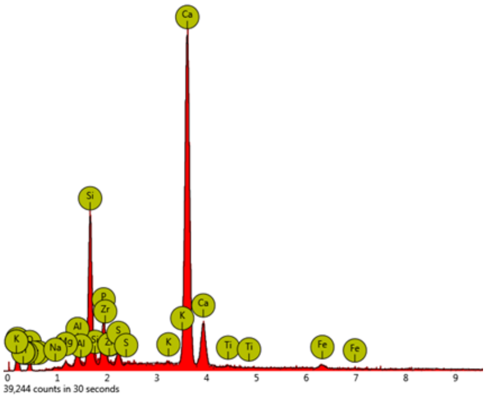

Fig. 10. SEM analysis result at 15% CBA

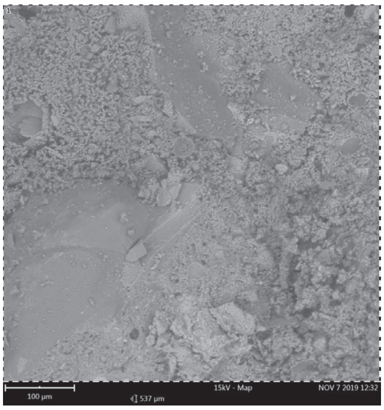

Element symbol	Atomic conc. [%]	Weight conc. [g]
Ca	44.44	59.11
Si	17.15	15.99
C	16.09	6.41
O	11.77	6.25
Fe	1.79	3.32
P	3.15	3.24
Al	1.94	1.73
S	1.63	1.73
Ti	0.38	0.61
Mg	0.66	0.54
K	0.39	0.50
Cl	0.27	0.32
Na	0.34	0.26

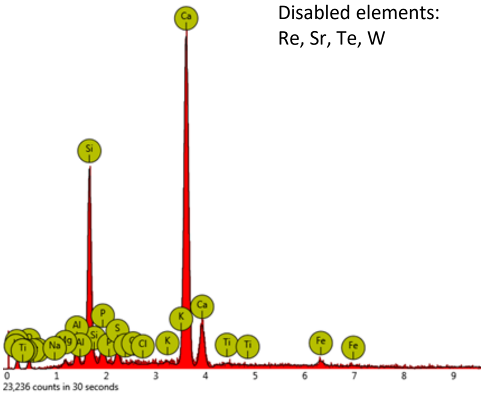

Fig. 11. SEM analysis result at 20% CBA

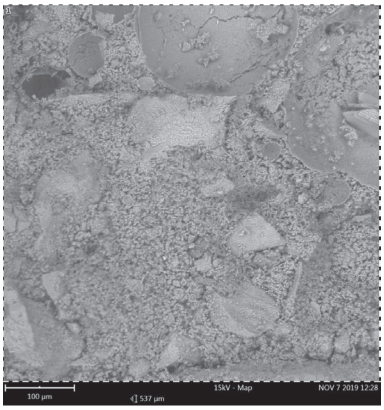

Element symbol	Atomic conc. [%]	Weight conc. [g]
Ca	64.43	70.93
Si	7.77	6.00
O	10.73	4.71
P	5.34	4.54
Zr	1.39	3.49
Fe	2.25	3.45
S	2.24	1.97
Al	2.24	1.66
Ti	0.71	0.93
Cl	0.79	0.77
Mg	1.07	0.71
K	0.40	0.43
Na	0.64	0.40

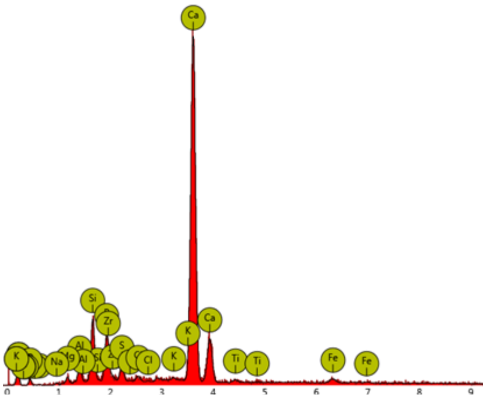

Fig. 12. SEM analysis result at 30% CBA

4. CONCLUSIONS

This study reveals that the replacement of cement with Cow Bone Ash of varying percentages (0%, 5%, 10%, 15%, 20%, 30%) affects the microstructural behavior of the concrete. The microstructural behavior in turn affects the strength and ASR characteristics of the concrete. Petrographic examination shows that the minimal and least amount of Alkali-Silica Reaction gels and microcracking were observed at 15% CBA replacement of cement in the concrete samples. These results can be related to the flocculation and discontinuation of gel production that occurs at 15% CBA production as the CBA has sealed up the cracks and inhibited gel production. Petrographic and SEM analysis reveals that, in the presence of CBA, aggregate reactivity are similar in terms of morphology to traditional Alkali-Silica Reaction gels, however, the amount of gels produced is small, as shown by the compact microstructure and negligible number of microcracks at 15% CBA replacement in the concrete samples. According to the Scanning Electron Microscopy (SEM) analysis, changes in the elemental composition of the concrete samples are related to the effect of CBA which enhances adhesion in the concrete. The microstructure analysis therefore concludes that pozzolanic reactions activated at 15% optimum CBA replacement by the presence of Cow Bone Ash (CBA) alters the elemental and microstructural properties of the concrete. This occurs by the release of Calcium Hydroxide (CH) and the production of additional Calcium Silicate Hydrate (C-S-H).

REFERENCES

[1] Jozwiak-Niedzwiedzka D., Dąbrowski M., Gibas K., Antolik A. & Glinicki M. (2018). Alkali-Silica Reaction and microstructure of concrete subjected to combined chemical and physical exposure conditions. *MATEC Web of Conferences*, 163(1–4), 1–10.

[2] Sharma A.K. (2019). Cracks in Pavement Quality Concrete (PQC) – Causes and Remedies. *International Advanced Research Journal in Science, Engineering and Technology*, 6(10), 40–48.

[3] Zapała-Sławeta Justyna & Owsiak Z. (2018). The use of lithium compounds for inhibiting alkali-aggregate reaction effects in pavement structures. *IOP Conference Series: Materials Science and Engineering*, 356, 1–10.

[4] Lawrence E.D. (2015). Flawed concrete found on Detroit Metro Airport runway. Detroit Free Press. Retrieved from: http://www.freep.com/story/news/local/michigan/wayne/2015/01/04/airport-needs-rebuild-million-runway/21236323/ [accessed: 14.10.2019].

[5] Holt E. & Ferreira M. (2013). *Addressing ASR in concrete construction in Finland.* In: Nord. Mini Seminar. Alkali Aggregate Reaction in Concrete, Riga, Latvia, 1–15.

[6] Tcherner J. & Aziz T.S. (2009). Effects of AAR on seismic assessment of nuclear power plants for life extensions. *20th International Conference on Structural Mechanics in Reactor Technology (SMiRT 20)*, Espoo, Finland, 9–14 August, 2009, (7-1789).

[7] Doran D., Douglas J. & Pratley R. (2009). *Refurbishment and repair in construction*. Whittles Publishing, Scotland, UK.

[8] Falade F., Ikponmwosa E. & Fapohunda C. (2012). Potential of pulverized bone as a pozzolanic material. *International Journal of Scientific & Engineering Research,* 3(7), 1–6.

[9] Adanikin A., Falade F.A. & Olutaiwo A.O. (2019). Efficiency of Cow Bone Ash (CBA) in mitigating alkali silica reaction (ASR) based on accelerated mortar bar test (AMBT) in concrete pavements. *UNILAG Faculty of Engineering International Conference on Managing the Environment (FEIC 2019).* 15–18 October, 2019, University of Lagos, Nigeria.

[10] Hassan M.S. (2014). SEM-Backscattered imaging analysis of cementitious composite matrix incorporating mineral admixture. *Engineering and Technology Journal*, 32(2), 696–703. Doi: 10.1590/s1517-707620170002.0145.

[11] Magudeswaran P. & Saran A.S. (2017). SEM analysis on sustainable high performance concrete. *International Journal of Innovative Research in Science, Engineering and Technology,* 6(6), 10237–10246. Doi: 10.15680/IJIRSET.2017.0606016.

[12] Balakrishnaiah D., Balaji K.V.G.D. & Srinivasa R.P. (2017). Application of SEM method to investigate the cause of effect of elevated temperatures on compressive strength for ternary blended concrete using metakaolin and micro silica. *ARPN Journal of Engineering and Applied Sciences*, 12(7), 2029–2036.

[13] Kumar S.V., Rajkumar R. & Umamaheswari N. (2019). Study on mechanical and microstructure properties of concrete prepared using metakaolin, silica fume and manufactured sand. *Rasayan Journal of Chemistry*, 12(3), 1383–1389. Doi: 10.31788/RJC.2019.1235164

[14] Uzbas B. & Aydin A.C. (2019). Analysis of fly ash concrete with Scanning Electron Microscopy and X-ray diffraction. *Advances in Science and Technology Research Journal,* 13(1), 100–110. Doi: 10.12913/22998624/114178.

[15] BS 1881-211 (2016). *Testing concrete. Procedure and terminology for the petrographic examination of hardened concrete* (British Standard).

[16] ASTM C1723 (2016). *Standard guide for examination of hardened concrete using Scanning Electron Microscopy*. Retrieved from: https://www.astm.org/Standards/C1723.htm [accessed: 25.07.2019].

[17] Chen P.-W., Fu X. & Chung D.D.L. (1997). Microstructural and mechanical effects of latex, methylcellulose and silica fume on carbon fiber reinforced cement. *ACI Materials Journal,* 94(2), 147–155.

[18] Liu D.J., Chen M.J., Xue L. & He F. (2018). The effect of carbon fiber on concrete compressive strength. *Advanced Materials Research*, 1145, 106–111.

[19] Kotaro D., Sachiko H., Hideki K. & Eiji A. (2018). Effects of oxygen pressure and chloride ion concentration on corrosion of Iron in mortar exposed to pressurized humid oxygen gas. *Journal of Electrochemical Society,* 165(9), 582–589.

[20] Qureshi M. & Barbhuiya S. (2016). Effects of silica fume on the strength and durability properties of concrete. *1st International Conference on Civil Engineering for Sustainable Development – Opportunities and Challenges (CESDOC 2016),* 19–21 December, 2016, Guwahati, Assam, India, 117–120.